

**AFRL-VA-WP-TR-2005-3075**

**A UNIFIED METHODOLOGY FOR  
AEROSPACE SYSTEMS INTEGRATION  
BASED ON ENTROPY AND THE  
SECOND LAW OF  
THERMODYNAMICS:  
AERODYNAMICS ASSESSMENT**



**José A. Camberos**

**Computational Sciences Branch (AFRL/VAAC)**

**Aeronautical Sciences Division**

**Air Vehicles Directorate**

**Air Force Materiel Command, Air Force Research Laboratory**

**Wright-Patterson Air Force Base, OH 45433-7542**

**Shohei Nomura**

**The University of Michigan**

**Jason Stewart and Richard Figliola**

**Clemson University**

**AUGUST 2004**

**Final Report for 24 May 2004 – 20 August 2004**

**Approved for public release; distribution is unlimited.**

**STINFO FINAL REPORT**

**AIR VEHICLES DIRECTORATE**

**AIR FORCE MATERIEL COMMAND**

**AIR FORCE RESEARCH LABORATORY**

**WRIGHT-PATTERSON AIR FORCE BASE, OH 45433-7542**

## NOTICE

Using Government drawings, specifications, or other data included in this document for any purpose other than Government procurement does not in any way obligate the U.S. Government. The fact that the Government formulated or supplied the drawings, specifications, or other data does not license the holder or any other person or corporation; or convey any rights or permission to manufacture, use, or sell any patented invention that may relate to them.

This report was cleared for public release by the Air Force Research Laboratory Wright Site Public Affairs Office (AFRL/WS) and is releasable to the National Technical Information Service (NTIS). It will be available to the general public, including foreign nationals.

PAO Case Number: AFRL/WS 04-0715, 01 Sep 2004.

THIS TECHNICAL REPORT IS APPROVED FOR PUBLICATION.

/s/

---

DAVID J. MOORHOUSE  
Project Engineer  
Multidisciplinary Technologies Center  
Structures Division

/s/

---

MICHAEL L. ZEIGLER  
Chief,  
Design & Analysis Methods Branch  
Structures Division

/s/

---

David M. Pratt, Ph.D.  
Technical Advisor, Structures Division  
Air Vehicles Directorate

This report is published in the interest of scientific and technical information exchange and its publication does not constitute the Government's approval or disapproval of its ideas or findings.

REPORT DOCUMENTATION PAGE					Form Approved OMB No. 0704-0188	
<p>The public reporting burden for this collection of information is estimated to average 1 hour per response, including the time for reviewing instructions, searching existing data sources, gathering and maintaining the data needed, and completing and reviewing the collection of information. Send comments regarding this burden estimate or any other aspect of this collection of information, including suggestions for reducing this burden, to Department of Defense, Washington Headquarters Services, Directorate for Information Operations and Reports (0704-0188), 1215 Jefferson Davis Highway, Suite 1204, Arlington, VA 22202-4302. Respondents should be aware that notwithstanding any other provision of law, no person shall be subject to any penalty for failing to comply with a collection of information if it does not display a currently valid OMB control number. <b>PLEASE DO NOT RETURN YOUR FORM TO THE ABOVE ADDRESS.</b></p>						
1. REPORT DATE (DD-MM-YY) August 2004		2. REPORT TYPE Final		3. DATES COVERED (From - To) 05/24/2004– 08/20/2004		
4. TITLE AND SUBTITLE A UNIFIED METHODOLOGY FOR AEROSPACE SYSTEMS INTEGRATION BASED ON ENTROPY AND THE SECOND LAW OF THERMODYNAMICS: AERODYNAMICS ASSESSMENT				5a. CONTRACT NUMBER In-house		
				5b. GRANT NUMBER		
				5c. PROGRAM ELEMENT NUMBER 0602201		
6. AUTHOR(S) José A. Camberos (AFRL/VAAC) Shohei Nomura (The University of Michigan) Jason Stewart and Richard Figliola (Clemson University)				5d. PROJECT NUMBER A03Q		
				5e. TASK NUMBER		
				5f. WORK UNIT NUMBER 0D		
7. PERFORMING ORGANIZATION NAME(S) AND ADDRESS(ES) Computational Sciences Branch (AFRL/VAAC) Aeronautical Sciences Division Air Vehicles Directorate Air Force Materiel Command, Air Force Research Laboratory Wright-Patterson Air Force Base, OH 45433-7542				8. PERFORMING ORGANIZATION REPORT NUMBER AFRL-VA-WP-TR-2005-3075		
9. SPONSORING/MONITORING AGENCY NAME(S) AND ADDRESS(ES) Air Vehicles Directorate Air Force Research Laboratory Air Force Materiel Command Wright-Patterson Air Force Base, OH 45433-7542				10. SPONSORING/MONITORING AGENCY ACRONYM(S) AFRL/VASD		
				11. SPONSORING/MONITORING AGENCY REPORT NUMBER(S) AFRL-VA-WP-TR-2005-3075		
12. DISTRIBUTION/AVAILABILITY STATEMENT Approved for public release; distribution is unlimited.						
13. SUPPLEMENTARY NOTES Report contains color.						
14. ABSTRACT We present a viscous computational fluid dynamics (CFD) simulation over two finite twisted wings configured so as to give a theoretically predicted elliptic and parabolic lift distributions. Local surface integration and farfield methods were used to calculate the induced drag. The objective of this project is to relate work-potential losses (exergy destruction) to the aerodynamics forces in an attempt to validate a new design methodology based on the second law of thermodynamics. Exergy destruction for the entire flow field was determined from the CFD results. CFD results show that the parabolic case produces smaller induced drag and entropy generation rates than the elliptic case. The entropy generation rates for both cases deviated significantly from the expected values, revealing the inaccuracy of entropy generation rate prediction for a turbulent flow. This project, however, set up a basis in terms of analysis methodology, from which the future work will follow.						
15. SUBJECT TERMS Entropy, Exergy, CFD, Aircraft, Design						
16. SECURITY CLASSIFICATION OF:			17. LIMITATION OF ABSTRACT: SAR	18. NUMBER OF PAGES 46	19a. NAME OF RESPONSIBLE PERSON (Monitor) David J. Moorhouse, Ph.D.	
a. REPORT Unclassified	b. ABSTRACT Unclassified	c. THIS PAGE Unclassified			19b. TELEPHONE NUMBER (Include Area Code) (937) 255-2123	

# TABLE OF CONTENTS

---

LIST OF FIGURES .....	iv
LIST OF TABLES .....	v
ABSTRACT .....	vi
FOREWORD.....	vii
SUMMARY .....	1
INTRODUCTION.....	2
OBJECTIVES .....	4
COMPUTATIONAL METHODOLOGY.....	5
GEOMETRY AND GRID GENERATION.....	6
Computational Domain .....	6
Classical Lifting-Line Theory .....	6
Constructing the Wing Geometry .....	10
Grid Generation .....	10
RESULTS .....	16
Validation of Grid Quality .....	16
Comparison of Lift and Drag with Lifting-Line Theory .....	17
Entropy Generation and Exergy Destruction Rate .....	19
DISCUSSION .....	22
CONCLUSIONS .....	24
FUTURE WORK .....	25
REFERENCES .....	33

# LIST OF FIGURES

<i>Figures</i>	<i>Page</i>
Figure 4.1. Overall view of computational domain .....	6
Figure 4.2. Wing tip vortex .....	7
Figure 4.3. Wing tip vortex from solution .....	8
Figure 4.4. Velocity Triangle .....	9
Figure 4.5. Wing geometry .....	10
Figure 4.6. $y^+$ contours on surface of the wing .....	12
Figure 4.7. Wing surface grid .....	13
Figure 4.8. Wing surface grid and the surrounding grid .....	13
Figure 4.9. Leading edge grid to tip transition grid .....	14
Figure 4.10. Overall wing tip mesh .....	14
Figure 4.11. Trailing edge tip grid .....	14
Figure 4.12. Slice through domain showing grid .....	15
Figure 4.13. View of cylindrical grid volume around wing .....	15
Figure 6.1. Region of high $y^+$ values .....	17
Figure 6.2. Pressure contour at $z = 2.9\text{m}$ for elliptic case .....	17
Figure 6.3. Schematic of Trefftz plane .....	18
Figure 6.4(a) Rolled up streamlines for elliptic case .....	26
Figure 6.4(b) Rolled up streamlines for parabolic case .....	26
Figure 6.5. Total entropy generation rate for elliptic turbulent case at $z = 0.5\text{m}$ ...	27
Figure 6.6. Total entropy generation rate for elliptic turbulent case at $z = 1.5\text{m}$ ...	27
Figure 6.7. Total entropy generation rate for elliptic turbulent case at $z = 2.9\text{m}$ ...	27
Figure 6.8. Total entropy generation rate at leading edge for elliptic turbulent case at $z = 2.9\text{m}$ .....	28
Figure 6.9. Total entropy generation rate at trailing edge for elliptic turbulent case at $z = 2.9\text{m}$ .....	28
Figure 6.10. Total entropy generation rate for elliptic case at $y = 0\text{m}$ .....	29
Figure 6.11. Total entropy generation rate for parabolic case at $z = 0.5\text{m}$ .....	29
Figure 6.12. Total entropy generation rate for parabolic case at $z = 1.5\text{m}$ .....	29
Figure 6.13. Total entropy generation rate for parabolic case at $z = 2.9\text{m}$ .....	30

Figure 6.14. Total entropy generation rate for elliptic case at $y = 0\text{m}$ .....	30
Figure 7.1. Induced drag coefficients at varying streamwise locations with varying Trefftz plane area (elliptic turbulent case) .....	30

## LIST OF TABLES

---

<i>Tables</i>	<i>Page</i>
Table 6.1. Induced and total drag coefficients .....	31
Table 6.2. Lift coefficients .....	31
Table 6.3. Drag and lift coefficients calculated with surface integration over the wing surface .....	31
Table 6.4. Expected total entropy generation rate and the results from the CFD simulations .....	32

# ABSTRACT

---

We present a viscous computational fluid dynamics (CFD) simulation over two finite twisted wings configured so as to give a theoretically predicted elliptic and parabolic lift distributions. Local surface integration and farfield methods were used to calculate the induced drag. The objective of this project is to relate work-potential losses (exergy destruction) to the aerodynamics forces in an attempt to validate a new design methodology based on the second law of thermodynamics. Exergy destruction for the entire flow field was determined from the CFD results. CFD results show that the parabolic case produces smaller induced drag and entropy generation rates than the elliptic case. The entropy generation rates for both cases deviated significantly from the expected values, revealing the inaccuracy of entropy generation rate prediction for a turbulent flow. This project, however, set up a basis in terms of analysis methodology, from which the future work will follow.

# FOREWORD

---

This report, “A Unified Methodology for Aerospace Systems Integration based on Entropy and the Second Law of Thermodynamics: Wing Aerodynamics Assessment”, gives a technical discussion of research accomplished to develop the methods to compute entropy generation rate of different wing sections and planforms. It is a part of a larger effort to develop the Second Law of Thermodynamics into the common currency for all aspects of system integration. This report considers the work that needs to be accomplished by a flight vehicle (e.g., the generation of lift to keep a body aloft at sea-level conditions), and identifies sources of inefficiency associated with finite wing aerodynamics.

The work was led by Prof. Richard Figliola of Clemson University guiding a team of graduate students, Mr. Jason Stewart of Clemson University and Mr. Shohei Nomura of the University of Michigan. The Air Force Office of Scientific Research sponsored the project under Program Manager Dr. John Schmisser. It was administered by the Air Force Research Laboratory, Air Vehicles Directorate with Dr. José Camberos as project advisor.

The work was accomplished during the period 24 May to 20 August 2004.

Dr. David J. Moorhouse  
Director, Multidisciplinary Technology Center  
AFRL Air Vehicles Directorate  
Wright-Patterson AFB, OH 45433





# SUMMARY

---

Using Air Force's in-house code, Air Vehicle Unstructured Flow Solver, we simulated the three dimensional, viscous, laminar and turbulent, low subsonic flows around the finite wings with theoretically predicted elliptic and parabolic lift distributions. The wings had a rectangular planform with geometric twists. Using the surface integration and the Trefftz plane methods, lift and the induced drag, respectively, were extracted for a comparison with the classical lifting-line theory. As expected, the results for the lift compared favorably with the theoretical values; they had errors of no more than 6%. The induced drag, on the other hand, experienced a maximum error of roughly 30%. We also attempted to perform both qualitative and quantitative analysis of the entropy generation rates and the exergy destruction rates. For both elliptic and parabolic cases, the boundary layer seemed to produce the majority of the entropy. We obtained the quantitative figures by taking the volume integral of the total entropy generation rates over the entire computational domain, including the wake. These results deviated significantly from the approximate values, which are simply the product of the total drag and the cruise velocity.

Using the classical lifting-line theory, we have established the basic techniques for building the twisted wing geometries with the desired lift distributions. The *actual* lift distributions of these wings yet require a validation. Nonetheless, we have also established a grid generation technique for such twisted wings. The implementation of the farfield induced drag extraction method to a viscous solution needs a further investigation. In particular, we will examine the effect of the location and the size of the Trefftz plane on the induced drag. As for the entropy generation study, we will investigate the concept of effective viscosity, which takes into account the turbulence effect lost in the Reynolds averaging in the Navier-Stokes equations.

Overall, the basis established during the summer of 2004 should provide a good starting point for the study of an exergy-based design methodology. The following major objectives include the grid refinement study and the investigation of the relationships between the aerodynamic inefficiencies with the irreversible losses.

# INTRODUCTION

---

## PROBLEM DEFINITION

An aircraft represents an intricate system composed of a number of interacting energy and non-energy based sub-systems. Research in aerospace engineering has focused on the complicated procedure of integrating such subsystems for some time. Historically, designers have applied the design and optimization procedure only at a subsystem level. For example, a typical objective function for the design of a wing has sought to minimize drag for a given lift distribution. Design of a propulsion system has aimed to maximize thrust while maintaining as high thermodynamic efficiency as possible. Integration of these components or subsystems, optimized separately, requires a great deal of experience and knowledge. In addition, this subsystem-level optimization may ensure the optimum configuration for each subsystem, but does not guarantee an optimum design for the entire vehicle as a whole.

As flight vehicles evolve, they carry more and more intricate components that require distribution of power from an energy source [1]. With the need to develop a revolutionary design and optimization methodology for such systems, the basic approach started to shift from subsystem-level to system-level over the last few years. The main questions asked include: Can we find a single common parameter that will hold across all components in all stages of design process? To approach this question, consider all the constituent components as the energy-consuming systems. One way or the other, they all have some inefficiencies, which can be considered in terms of energy used for work versus energy wasted [1]. The answer therefore seems to lie in this concept of irreversible losses that is an additive quantity. So, can we design a flight vehicle based not only on the first law of thermodynamics, but also on the second law of thermodynamics? We seek to implement the second law of thermodynamics to provide a common metric that enables a comparison of the performance of different subsystems in terms of energy utilization, and to map in detail the location of all irreversible losses. We find a growing consensus in the literature [2,3,4,5,6] that this should lead to the further advances of air vehicle design methodology and to a true system-level optimization.

As part of this system-level aerospace vehicle analysis and design concept, the project presented in this report focuses on the aerodynamics of low subsonic viscous flow over a finite wing. Flow over a finite wing has been known to produce number of interesting phenomena. Examples are tip vortex and trailing vortices that cause additional induced drag. A major portion of this project seeks to predict this induced drag and the corresponding aerodynamic losses using a 3D viscous computational fluid dynamics (CFD) simulation.

This task, however, does not come so easy. In 3D viscous flow, a variety of sources subject the wing to an assortment of aerodynamic drag. One of these, skin friction drag, results from the viscosity of air and from velocity gradients near the wing surfaces. Another, the induced drag mentioned above, results from the generation of lift and downwash velocity as generated by the trailing and tip vortices. Form drag constitutes another type of drag resulting from an unbalanced pressure distribution around the wing and of viscous action. In addition to all these drag components, the inaccuracy of a CFD calculation appears as a spurious drag. The challenging task of extracting induced drag from a CFD calculation

comes from the difficulties encountered in numerically distinguishing each drag source from one another. This research project placed an emphasis on developing the induced drag extraction methods in context of our overall objective to apply the second law of thermodynamics.

Studying the energy efficiency in terms of second law of thermodynamics will help to analyze the lost work-potential that can otherwise perform useful work. This thermodynamic quantity, known as “exergy” or “availability”, represents the maximum theoretical work that can be obtained from a system in taking it from a given chemical composition, temperature, and pressure to a state of chemical, thermal, and mechanical equilibrium with the environment [7]. For example, the fuel supplied to an aircraft represents its exergy or maximum work potential. To meet the mission requirements, exergy consumption (destruction) must occur. Destruction of exergy during any chemical or physical process equals the irreversible losses – entropy generation scaled by a reference temperature. The second law of thermodynamics suggests that we should not necessarily strive to converse energy, but rather we should attempt to conserve exergy [8]. In the flow over a flight vehicle, minimizing the exergy destruction saves the available energy for distribution to other components of the aircraft for other types of useful work.

The authors of this report will study these concepts mentioned above using twisted finite wings configured to produce two limiting (spanwise) lift distributions; elliptic and parabolic. These two special cases provide a good starting point for exploring new territory, since they are known to have special characteristics. An elliptic lift distribution supposedly produces minimum induced drag, according to Prandtl’s classical lifting-line theory. A parabolic lift distribution gives another special case suggested by Greene [9] to have minimum entropy generation. For the elliptic lift distribution in particular, classical theory makes some major approximations, making it an interesting study. This project could serve as a numerical experiment to test the limits of validity of the well known theory. This report aims to present the contributions made thus far, the current status, and a number of suggestions for future work.

# OBJECTIVES

---

The objectives of this project come in several parts. Our first objective deals with the construction of twisted wing geometries with theoretically predicted lift distributions. Classical lifting-line theory provides the analytical expression for the required spanwise twist angle to produce a desired lift distribution. For our second objective, we seek basic grid generation techniques for constructing such twisted wings. We attempt to resolve the wake, as well as the turbulent boundary layer all the way down to the wing surface. These two preparations lead to the simulation of 3D, viscous, low subsonic, incompressible flow using the Air Force Research Laboratory's in house code, Air Vehicle Unstructured Flow Solver (*AVUS*) developed by the Computational Sciences Branch (AFRL/VAAC) over the past decade [11]. Lastly, the post-processing provides the visualization of the flow field, lift and drag forces, and entropy generation and exergy destruction rates. This project should serve as a validation study for the classical lifting-line theory and a hypothesis developed by Greene [9]. We also propose to establish a solid basis for the development of a design and optimization methodology based on the second law of thermodynamics.

# COMPUTATIONAL METHODOLOGY

---

We created the wing geometries and the grid using *Gridgen* version 15.03 (we give a brief description of how the grids were created below). The CFD code *AVUS* is a cell-centered finite-volume code. Its fundamental algorithm utilizes a scheme of first order accurate in space and time, and the grid-aligned exact Riemann solution method of Gottlieb and Groth [11]. The second order accurate spatial approximation method utilizes van Leer's MUSCL scheme. For an accelerated convergence, *AVUS* uses a local time stepping algorithm for steady state solutions. However, the low speed cases ( $M \leq 0.2$ ) with large jumps in spacing and/or cell size may require time-accurate calculations [11]. Because of computational constraints, our grid suffered from large jumps in cell size, so, we attempted to achieve a steady state solution using the time accurate option. Implementing the time accurate solver did not, however, yield fully converged solutions. Poor grid quality in certain regions may have contributed to this. The computational constraints put a limit on cell count and consequently yielded non-ideal grids.

We attempted to obtain solutions from both laminar and turbulent calculations with the Wilcox  $k-\omega$  model. Wilcox  $k-\omega$  model is a two-equation Reynolds Averaged Navier-Stokes (RANS) type model, which performs well in the near-wall region. From these simulations, we investigated the effect of turbulence model on the results.

The flight conditions used for this study are at a pressure of 1atm and temperature of 288K (sea-level), at a steady cruise Mach number of 0.2. The wing has a rectangular planform with an aspect ratio of 6 and a constant NACA0012 airfoil section of 1m chord, and a span of 6m. The wing has an assumed weight of 7300 N.

# GEOMETRY AND GRID GENERATION

---

## COMPUTATIONAL DOMAIN

Since the wing load and the flow field are symmetric about mid-span of the wing for a level flight, the computational domain includes only a half of the wing with one boundary condition set as the plane of symmetry. A total of seven faces formed the computational domain (Figure 4.1). We set all faces as the far-field boundary condition, except the wing surface and the face that splits the mid span of the wing. We labeled this mid-span face as the symmetry face and modeled it with as a solid wall with slip boundary conditions. The wing surfaces have no-slip wall boundary conditions. The outer faces that enclose the wing extends ten chord lengths behind the wing, five chord lengths above and below the wing, five chord lengths in front of the wing, and two span lengths in width.

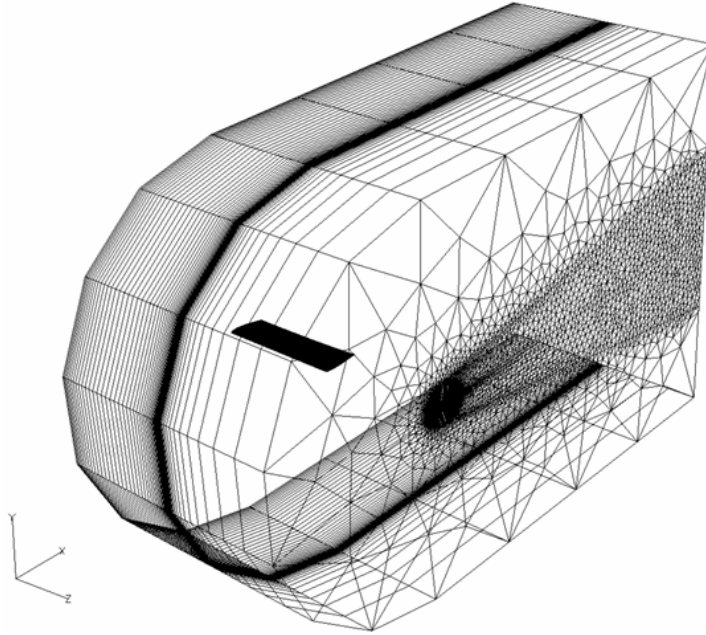


*Figure 4.1:* Overall view of the computational domain

## CLASSICAL LIFTING-LINE THEORY

Our intent was to construct a wing that produced an elliptic and parabolic lift distribution along the spanwise direction as two separate cases to test against classical lifting-line theory. The elliptic lift distribution supposedly produces minimum in induced drag. Greene [9] suggests that a parabolic lift distribution produces minimum entropy with an optimal bending moment at the root. Therefore, we are testing the hypothesis that a design that minimizes drag and a design that minimizes entropy production are not the same thing.

In the classical lifting-line theory, the lift distribution varies as a function of the effective angle of attack, the spanwise chord distribution, and the aerodynamic twist. In this project, chord stays constant along the span and the wing has no aerodynamic twist. Hence, the lift distribution becomes a function of the effective angle of attack in the spanwise direction only.

When a finite wing produces lift, its effective angle of attack is less than the geometric angle of attack, the angle between the free stream velocity vector and the chord line. A high pressure region exists on the lower surface relative to the upper surface of the wing. At the wing tip, the lift must be zero, and therefore the upper and lower pressures must equate. Consequently, the flow at the tip tends to move from the high pressure region on the lower surface to the lower pressure region on the top. This causes a spanwise flow component along the entire wing span. Effectively, the wing suffers from a decreased lift coefficient and an increased drag coefficient relative to the two-dimensional case (or an infinite wing case).

This spanwise flow creates the wing tip vortices (Figure 4.2 and 4.3). Since the fluid on the lower surface of the wing tends to flow outward toward the tip and the fluid on the upper surface tends to flow inward toward the root, a trailing vortex forms when these two flows meet at the trailing edge. The trailing vortex across the wing span creates a vortex sheet, which induces a downwash velocity given by

$$w(z) = -\frac{1}{4\pi} \int_{-b/2}^{b/2} \frac{\Gamma'(z)}{z_0 - z} dz \quad (4.1)$$

where  $\Gamma(z)$  is the circulation distribution along the span,  $U_\infty$  is the free stream velocity, and  $b$  is the total span length. This downwash velocity effectively reduces the approach angle of the free stream velocity vector by an amount of induced angle. The effective angle of attack equals the difference in the geometric and induced angles.



Figure 4.2: Wing Tip Vortex (Picture from DANTEC Measurement Technology)



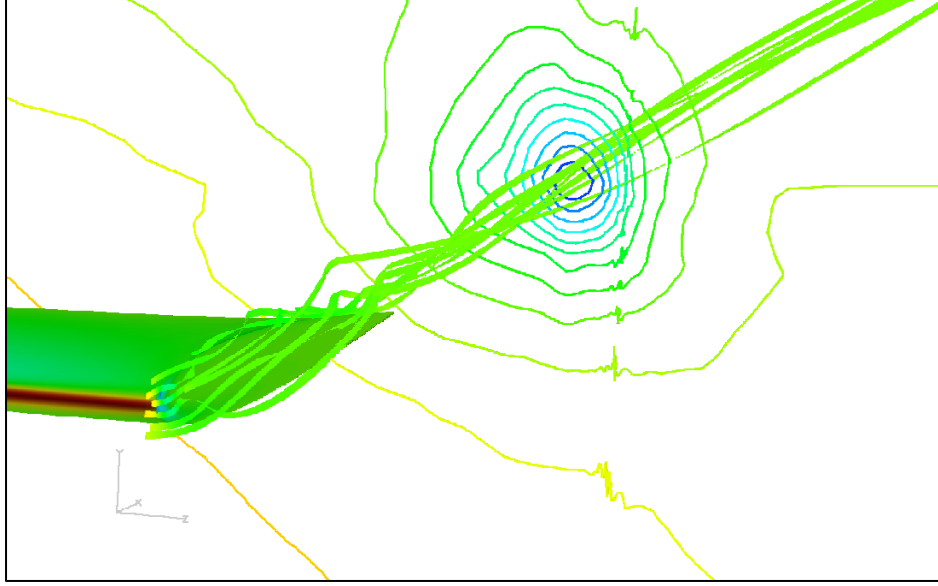


Figure 4.3: Wing tip vortex from CFD solution

We can achieve a particular lift distribution by giving the wing a geometric twist, an aerodynamic twist, or a combination of both. Geometric twist refers to a variation in the geometric angle of attack whereas aerodynamic twist refers to varying the airfoil sections. We chose the geometric twist for this project for the relative ease of geometry and grid generation. The equation of lift coefficient,

$$L(z) = \frac{1}{2} m_0 U_\infty^2 \rho c \alpha_0(z) \quad (4.2)$$

indicates that the effective angle of attack,  $\alpha_0$  must follow the same trend as the desired lift distribution, since the lift slope  $m_0$  ( $2\pi$  according thin airfoil theory), freestream density  $\rho$ , chord  $c$ , and the freestream velocity  $U_\infty$  stay constant. For instance, in order to obtain an elliptic lift distribution,  $\alpha_0$  must vary in an elliptic fashion as well. The choice of the root effective angle of attack is mission-specific. For an elliptic case, we chose an arbitrary root effective angle of attack of  $5^\circ$ , which corresponds to an assumed aircraft weight of about 7300N.

The induced angle refers to the change in approach angle experienced by the free stream velocity due to the downwash velocity discussed earlier. From geometry (Figure 4.4), downwash angle ( $\alpha_i$ ) is simply

$$\alpha_i(z) = \tan^{-1} \frac{w(z)}{U_\infty} \quad (4.3)$$

which simplifies to

$$\alpha_i(z) = \frac{w(z)}{U_\infty} \quad (4.4)$$

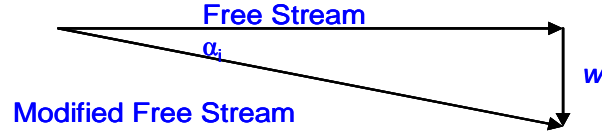


Figure 4.4: Velocity Triangle

for a small downwash velocity compared to the freestream velocity. For an elliptic lift distribution, the induced angle of attack stays constant along the span:

$$\alpha_i = -\frac{\Gamma_0}{2bU_\infty} \quad (4.5)$$

Here,  $\Gamma_0$  is the root circulation, determined from the  $5^\circ$  root effective angle by

$$\Gamma_0 = \frac{m_0 c U_\infty \alpha_0}{2} \quad (4.6)$$

Now, the geometric angle as a function of span can be determined by

$$\alpha(z) = \alpha_0(z) + \alpha_i(z) \quad (4.7)$$

The resulting function for the geometric angle of for an elliptic lift distribution with a  $5^\circ$  effective root angle is then

$$\alpha(z) = \alpha_{root} \sqrt{1 - \left(\frac{z}{b/2}\right)^2} \quad (4.8)$$

where  $\alpha_{root}$  is a root geometric angle of attack of  $6.30899^\circ$ .

In order to have an accurate comparison, both elliptic and parabolic wings must produce the same total amount of lift. This requires that the area under a curve of effective angle of attack vs. wing span should be equal when both wings are flying under the same flow conditions. Therefore,

$$\int_{-b/2}^{b/2} 5^\circ \sqrt{1 - \left(\frac{z}{b/2}\right)^2} dz = \int_{-b/2}^{b/2} \alpha_0 \left(1 - \left(\frac{z}{b/2}\right)^2\right) dz \quad (4.9)$$

Solving this equation yields the root effective angle of  $5.89049^\circ$  for the parabolic case. The induced angle of attack as a function of span for the parabolic case turns out to be

$$\alpha_i(z) = -\frac{2\Gamma_0}{b^2\pi U_\infty} \left( -b + z \ln \left( \frac{\left| z + \frac{b}{2} \right|}{\left| z - \frac{b}{2} \right|} \right) \right) \quad (4.10)$$

This equation indicates that the induced angle of attack approaches negative infinity as  $z$  approaches  $b/2$  (wing tip). Obviously, this presents a problem when building the wing geometry. To overcome this problem the slope of the geometric angle of attack curve at 99.7 % of the span was used to extrapolate out to the tip. This resulted in a root geometric angle of attack of  $7.85398^\circ$  and a tip geometric angle of attack of  $-4.99262^\circ$  for an overall geometric twist of  $12.85^\circ$ . Interestingly, the parabolic case has the negative tip geometric angle of attack. Nonetheless, both effective angles at the wing tip should be  $0^\circ$ .

### CONSTRUCTING THE WING GEOMETRY

The wings were constructed using a straight leading edge that has no slope in any direction. We attached the airfoil sections to the leading edge, rotated the proper amount to give the desired geometric angle of attack. Once we placed an appropriate number of airfoils, an interpolating scheme in *Gridgen* was used to create the surface between the airfoil sections. Figure 4.5 shows an example of the wing geometry.

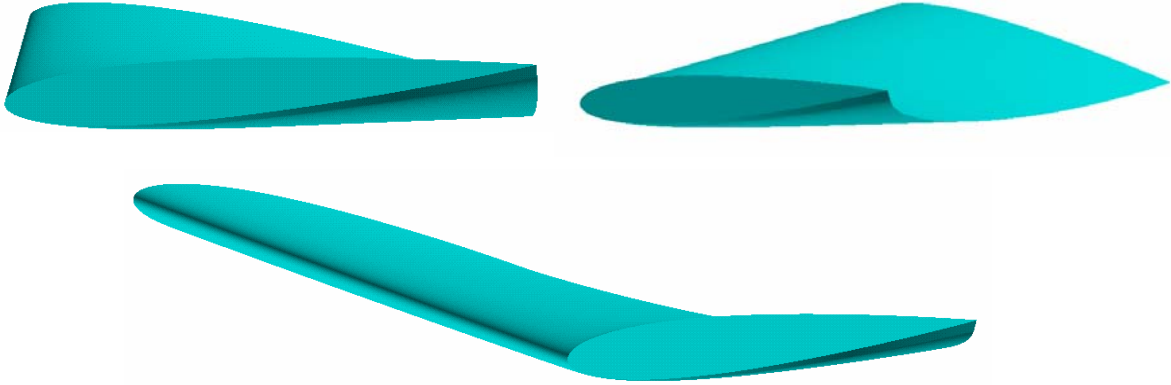


Figure 4.5: Twisted Wing Geometry

### GRID GENERATION

Constructing a proper grid perhaps takes up the most essential part of a CFD simulation. Grid construction unfortunately remains more of an art than a science and consequently requires a significant amount of time to develop a proper grid to adequately resolve the essential flow physics. Therefore, studying the flow field a priori is essential, especially when the solution-adaptive grid refinement is not available. Overall, the grid is

hybrid, consisting of the structured hexahedral cells in the boundary layer, and the unstructured prism-shaped cells elsewhere.

In a viscous solution one obvious place that requires a fine grid resolution is in the boundary layers. There are some guidelines to ensure the adequate resolution in this region. For the flow conditions for this study, the boundary layer will experience a transition from laminar to turbulent at roughly ten percent of the chord from the leading edge. Because of the very high gradients at the surface of the wing, especially for turbulent regions, it is necessary to cluster the cells in that region.

In a turbulent boundary layer there exists a laminar viscous sublayer that extends from the wall out to  $y^+$  (a normalized distance that is a function of shear stress) of about five. The first node distance from the wall should have a  $y^+$  value of one or less when using a two-equation turbulence model. This ensures that at least a few cells will describe the viscous sublayer. Determination of the first node distance from the wall starts from the flat plate boundary layer approximation. First the Reynolds number based on chord length must be determined:

$$\text{Re} = \frac{U_\infty c}{\nu} \quad (4.11)$$

This Reynolds number automatically determines the skin friction coefficient with the empirical correlation (for turbulent flow):

$$c_f = \frac{0.0592}{\text{Re}^{0.2}} \quad (4.12)$$

Using this value for the skin friction coefficient, the shear stress at the wall is then

$$\tau_w = \frac{1}{2} c_f \rho U_\infty^2 \quad (4.13)$$

With this shear stress approximation, the friction velocity can be found:

$$u^* = \sqrt{\frac{\tau_w}{\rho}} \quad (4.14)$$

Now the first node distance is obtained by setting  $y^+$  equal to one in the equation relating friction velocity to  $y^+$ :

$$y = \frac{\nu y^+}{u^*} \quad (4.15)$$

Using above relations, we see that the necessary first node distance is roughly  $5 \times 10^{-6}$  m. A problem arises with such a small length is used to construct a cell since the volume is now about  $10^{-18}$  m. This may increase truncation error significantly, and the computer may easily treat this volume as practically zero. In fact, the CFD utility code used to check grid quality for *AVUS*, *Blacksmith*, flags such a grid as unacceptable if this first node distance is used. To overcome this problem, we scaled up the entire model 100 times and used the CGS

(centimeter, gram, second) units when executing AVUS. Figure 4.6 shows the resulting  $y^+$  contour plots on the wing surface.

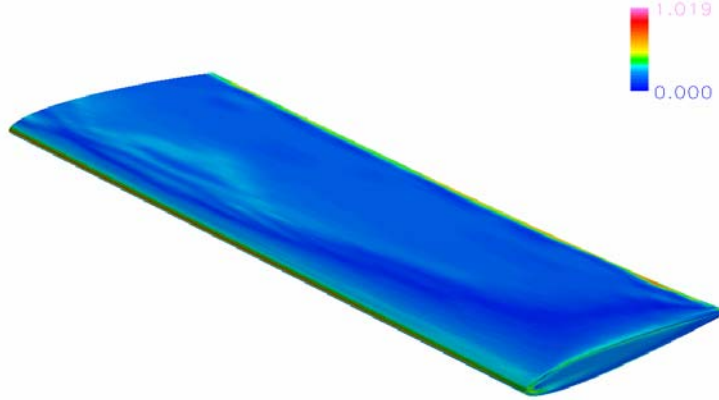


Figure 4.6: Normalized distance,  $y^+$  contours on the surface of the wing.

It has been suggested that roughly 150 to 200 points chordwise on both the top and bottom of the wing should suffice for an accurate drag prediction when used in conjunction with the other parameters concerning the boundary layer grid [10]. The leading and trailing edge require clustering of the grids. This allows the grid to accurately resemble the smooth curvature and provides a good transition between cells on the trailing edge and those in the near-wake. The first node distance of 0.450mm on the leading edge was taken from [10]. We also rounded the sharp trailing edge to facilitate the grid generation on the wing tip and the near-wake. To accurately trace this small curvature, a first node distance of 0.006 mm was used on the trailing edge.

Within the high-gradient regions like the boundary layer, the growth rate of the cells also plays an important role. It is suggested that the growth rate should at most be 20–30% [10] to avoid a significant error associated with the gradient calculations. Another generally accepted rule-of-thumb is to have at least ten cells within the boundary layer normal to the wall. We approximated the boundary layer thickness at a tenth of the chord, using the Blasius solution for the flat plate laminar boundary layer:

$$\delta = 5 \sqrt{\frac{\nu x}{U_\infty}} \quad (4.16)$$

The flat plate laminar boundary layer solution was used here since this is approximately the transition location from laminar to turbulence. Using this analytical solution gives a normal distance in which 10 cells should be placed. However, when considering the first node distance and a growth rate of 1.2, there will be more than 10 cells in the boundary layer at this location. Even with the turbulence models assuming a turbulent boundary layer over the entire wing, the grid-stretching scheme ensures 10 cells within the boundary layer.

Another important parameter in the boundary layer grid generation is the number of nodes along the span of the wing. It was suggested through a personal correspondence [10] that 100 points spanwise would be a reasonable number to start with. However, since the grid points need to be clustered at the wing tip, the number of required grid points could rise to about 200. The reason for the clustering at the wing tip is to allow for a good spanwise

transition from a wing tip boundary layer grid. In this project, however, we could only afford eighty nodes due to computer resource limitations. A view of the surface grid on the wing is shown in Figure 4.7 and 4.8.

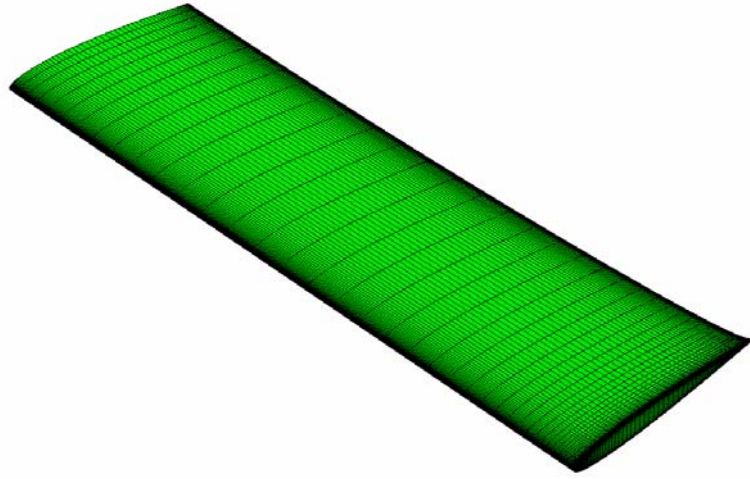


*Figure 4.7: Wing Surface Grid*

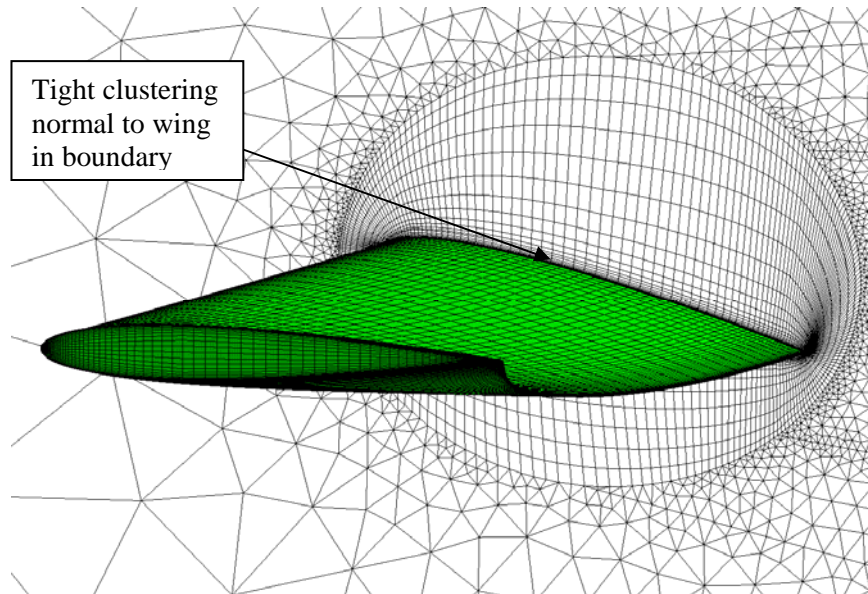


*Figure 4.8: Wing Surface Grid and Surrounding*

The wing tip presents a difficulty when producing a high quality structured grid. Having a sharp trailing edge results in highly skewed cells that could adversely affect convergence of the solution. Therefore, we rounded off the trailing edge at 99.75% of the chord to facilitate the grid generation procedure. Since the wing tip region will contain complicated flow, the boundary layer mesh and the wing tip mesh should have as smooth transition in size as possible. An illustration of this is shown in Figure 4.9. Figure 4.10 and Figure 4.11 show the overall wing tip grid and trailing edge tip grid, respectively. The wing tip was divided into several sections to create the grid shown in Figure 4.10. Again, an

affordable grid count was limited by computer resources. Therefore, the grid suffered from discontinuous jumps in size, which are apparent in Figure 4.11.

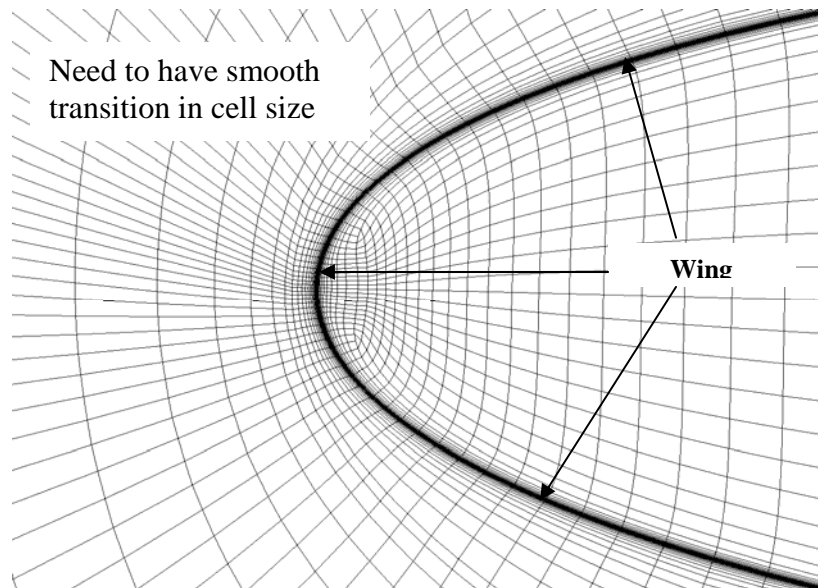


Figure 4.9: Leading Edge Grid to Tip

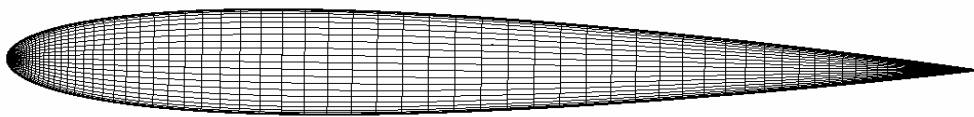


Figure 4.10: Overall Wing Tip Mesh

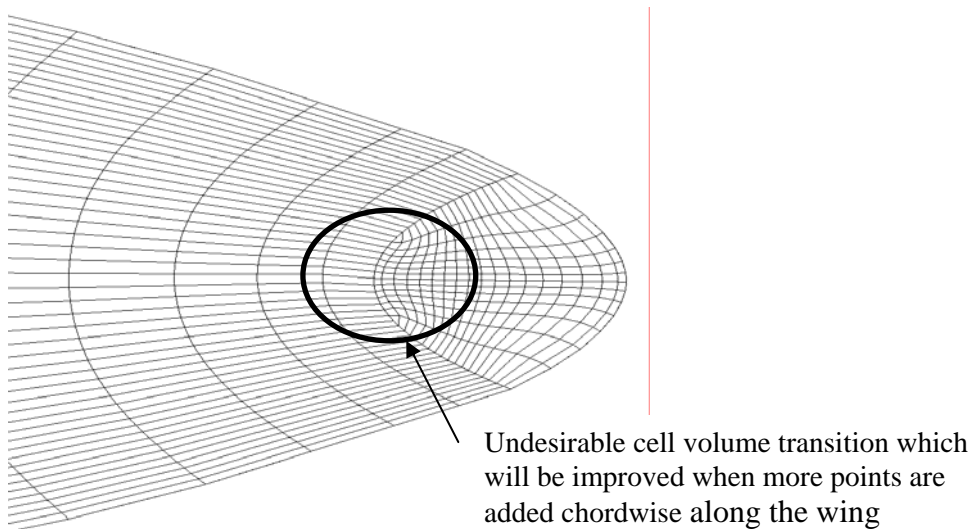


Figure 4.11: Trailing edge tip grid



The trailing vortices in the wake can be resolved effectively with the unstructured grid without increasing the cell count significantly (Figure 4.12). Here, the grid is clustered in the wake and grows quickly to the outer region. We approximated the growth rate of the wake height as  $2x^{1/3}$  [13] where  $x$  is the streamwise location.

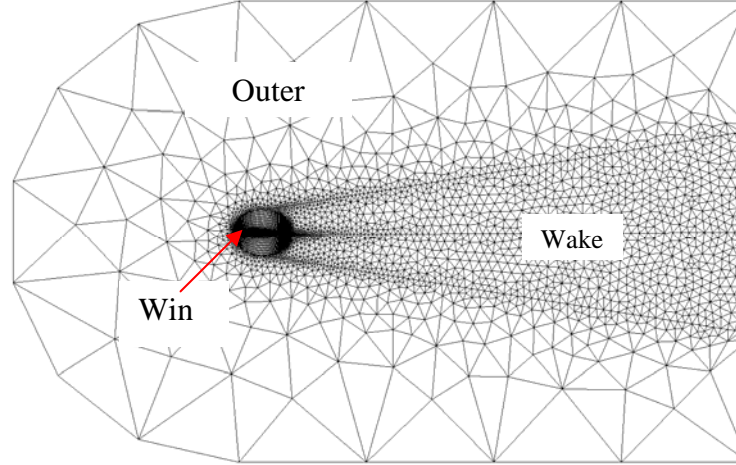


Figure 4.12: Slice through domain showing grid

A structured cylindrical grid was also constructed around the wing on top of the structured boundary layer grid. The surface of the boundary layer grid follows the twist of the wing in order to maintain a constant node distance from the surface of the wing. This does not provide a uniform surface to sweep a face along to create a volume grid for the outer region. Therefore, we placed a cylindrically shaped structured grid to provide a uniform surface. A close up view of this grid is shown in Figure 4.13.

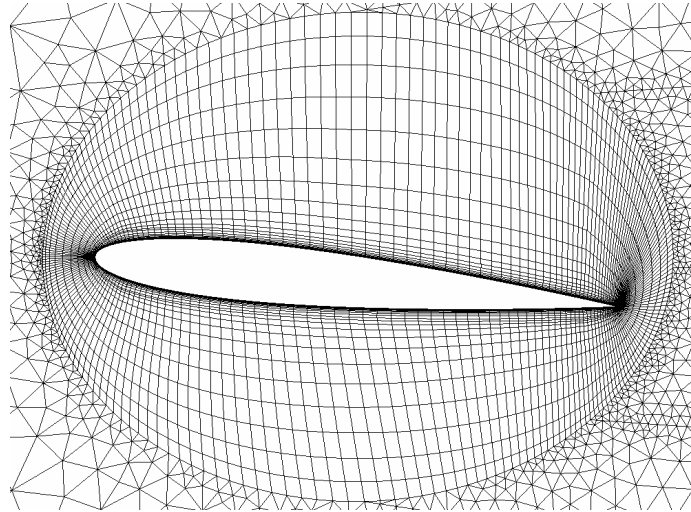


Figure 4.13: Cylindrical grid around the wing

Once we generated the grid for the half of the domain containing the wing, the volume grid was completed by simply sweeping all faces that lie in the mid plane of the domain, including the wing tip grid, in a linear fashion.



# RESULTS

---

Following accepted guidelines for the grid generation resulted in a total cell count in the order of several million. However, slow computational speed hindered the calculations from reaching full convergence within the given time limit. The machines used for all the calculations consisted of a Linux-based Beowulf cluster of Pentium III 800MHz processors each with 1GB RAM. The cluster contained sixty four processors in total and we used the maximum of thirty processors for any given job. Executing *AVUS* on thirty processors to solve incompressible viscous flow on a grid with 3.6 million cells, for example, took roughly thirty minutes per iteration. Reasonable convergence generally required at least 5000 iterations. Therefore, to achieve satisfactory convergence at this rate would require nearly 104 days.

To obtain results in a reasonable time, it was necessary to coarsen the grid. In addition, we increased the growth rate of the cell size as much as possible and coarsened the wake region as well. We filled the outer region with a very coarse grid to reduce the number of cells as much as possible, so the growth rate in this region exceeds 1.3. After this grid coarsening process, the total cell count dropped down to 1.79 and 1.87 million for the elliptic and parabolic wing, respectively. With cell count of 1.87 million, for example, it took roughly four days to complete 3800 iterations.

For every simulation, we let twenty processors work in parallel to solve the flow as close to full convergence as possible to a steady state under low subsonic condition ( $M=0.2$ ,  $Re_c=4,400,000$  and standard temperature and pressure). Residuals for continuity,  $y^+$ , and forces in the  $x$  and  $y$  direction respectively,  $F_x$  and  $F_y$ , were monitored during the calculation to check the convergence status. However, grid quality hampered the calculations from reaching full convergence. Therefore, we attempted to bring the solutions as close as possible to full convergence. On average, it took roughly 5000 iterations for  $y^+$  residuals to level off, but the force components in the  $x$ -direction continued to exhibit large oscillations, even after 10,000 iterations.

## VALIDATION OF GRID QUALITY

To verify grid resolution one may check the  $y^+$  values on the wing surfaces, which should be less than unity. Contours of  $y^+$  showed that for both elliptic and parabolic cases,  $y^+$  values stayed well below one on all wing surfaces, except at the very small region towards the tip (Figure 6.1), where it exceeded two. Although these high  $y^+$  values lie in such a tiny strip of surface that they may not be affecting the lift and drag values significantly, we suggest that the first grid size normal to the wing surface in these areas should be reduced.

Figure 6.2 shows the pressure contour around the sectional plane at  $z = 2.9\text{m}$  for the elliptic case. Non-smooth contour lines in the outer regions indicate the under-resolved flow. These regions require further grid refinement in future work, since they could affect the solution in the vicinity of the wing surface.

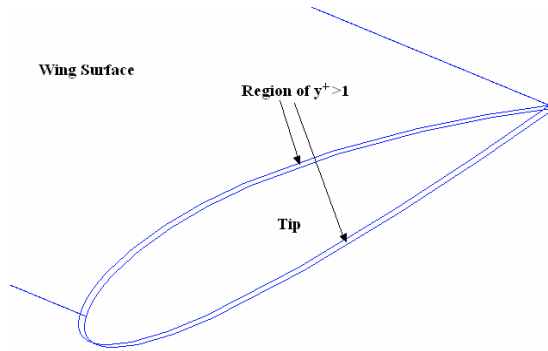


Figure 6.1: Region of high  $y^+$  values

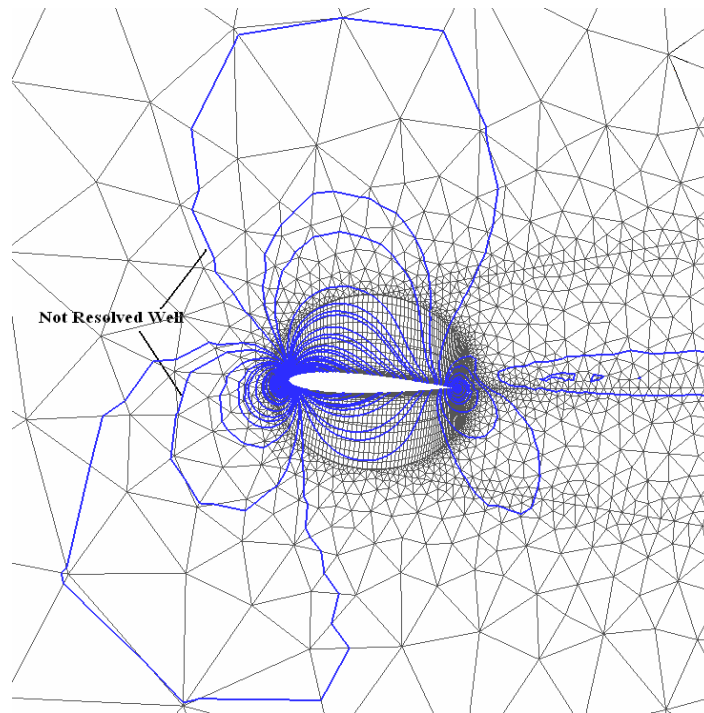


Figure 6.2: Pressure contour at spanwise location  $z = 2.9\text{m}$  for elliptic

## COMPARISON OF LIFT AND DRAG WITH LIFTING-LINE THEORY

One of the objectives of this project is to predict induced drag and compare with the theoretical values from lifting-line theory. However, prediction of aerodynamic forces, especially drag prediction is a very difficult task. Therefore, we are in a sense testing the capabilities of aerodynamic force prediction of CFD.

There exist several different methods for predicting aerodynamic forces. A typical method of calculating total drag and lift forces is the surface integration technique, in which

the pressure and the skin friction are integrated over the solid surfaces. Often times, using this method yields an accurate lift prediction, but faces difficulties in total drag prediction. This inaccuracy comes from the need to approximate the smooth curvature of the object with flat cells and to numerically approximate high gradients [14] in the boundary layer. These approximations lead to production of spurious contributions to drag as well, which appears in pressure and skin friction over a body surface. Therefore, spurious contribution cannot be differentiated from the physical drag by the surface integration method [15].

We therefore implemented the farfield analysis of Trefftz plane for the induced drag extraction. Formulating momentum conservation equations for the control volume that encloses the entire wing leads to the following simple integral to be taken over the cross-flow plane (Trefftz plane) at a downstream location of the wing (Figure 6.3):

$$D_i = \frac{1}{2} \rho_\infty \int v^2 + w^2 dS \quad (6.1)$$

Here,  $v$  and  $w$  are the lateral velocity perturbations. This integral simply sums the lateral kinetic energy across the Trefftz plane. The idea is that this lateral kinetic energy is caused purely by trailing vortices, the reversible phenomena that are the source of induced drag. This equation assumes the negligible streamwise velocity perturbations at the location of the Trefftz plane.

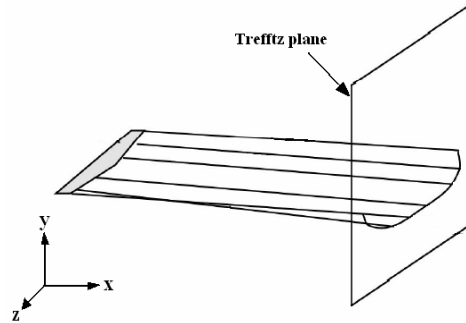


**Figure 6.3:** Schematic of Trefftz plane

Many researchers have applied Trefftz plane method to the inviscid case frequently and obtained fairly accurate drag and lift results. In an inviscid case, the location of the Trefftz plane is not important, as long as the streamwise velocity perturbation can be considered negligible, and the plane encompasses the entire laterally-perturbed area.

However, when it is applied to the viscous case, computation gets more difficult because of the natural viscosity of the fluid that tends to damp out these lateral motions. In addition, the artificial viscosity embedded in the numerical scheme itself also contributes to the dissipation of the solution in the wake, especially where the grid gets coarse. Therefore, the location of Trefftz plane should be where the flow experiences as little influence from the artificial viscosity as possible. In this project, we placed it at six chord-lengths downstream of the wing.

Table 6.1 shows the result for the induced drag coefficient from the lifting-line theory, as well as the results from the CFD calculation. Total drag coefficients from the surface integration method are also tabulated for comparison. It is apparent that the CFD calculation under-predicted the theoretical values. This may be due to the dissipating transverse kinetic energy, which is a consequence of both natural and artificial viscosity. It also predicted the induced drag for the parabolic cases to be smaller than the elliptic cases. This contradicts with the classical theory that says elliptic lift distribution produces minimum induced drag.

Table 6.2 shows the result for lift coefficient calculated by surface integration over the wing surface. Elliptic and parabolic cases have the same theoretical values, since the wings were designed to have the same total lift and they have the same wing surface area. Lift coefficient values are more accurate than the induced drag values.

One important point about the classical lifting-line theory is that the derivation of minimum induced drag for elliptic lift distribution assumes a planar vortex sheet that extends to infinity (inviscid approximation). In actual flow over a finite wing however, the vortex sheet rolls up out-of-plane (Figure 6.4 and 6.5) and dissipates because of viscous effect. Although classical lifting-line theory is shown to provide surprisingly accurate induced drag distribution [9], we should not exclude this approximation from the list of possible reasons for differences when comparing theoretical and predicted induced drag.

## **ENTROPY GENERATION AND EXERGY DESTRUCTION RATE**

The most important objective of this project was to test the capabilities of CFD to calculate the entropy generation and the exergy destruction rates and relate them to the aerodynamic terms, such as lift and drag. AVUS calculates the total entropy generation rate in every cell for viscous flow by

$$\dot{S}_{gen} = \frac{\tau_{ij}}{T} \frac{\partial u_i}{\partial x_j} - \frac{q_j}{T^2} \frac{\partial T}{\partial x_j} \quad (6.2)$$

and we normalized it as follows:

$$\dot{S}_{gen}^* = \dot{S}_{gen} \left[ \frac{T_0 L}{\rho_0 c_0^3} \right] \quad (6.3)$$

In equation 6.2, the first and the second term corresponds to the viscous and heat entropy contribution to the total entropy generation rate. For low subsonic incompressible flow, temperature gradients will be minimal. Therefore the majority of the contributions will come from the viscous term. Temperature gradients are calculated indirectly from density and pressure.

Figure 6.5 – 6.10 are the contour plots of the total entropy generation rate for the elliptic turbulent case. As expected, the boundary layer, leading edge region and the near wake produces the highest entropy generation rate (Figure 6.8 and 6.9). Entropy generation rate in the region indicated by blue is essentially zero.

Figure 6.11 – 6.14 show the contour plots of total entropy generation rate for the parabolic turbulent case. This wing produced a similar total entropy generation rate plot as compared to the elliptic case.

Although majority of the entropy generation happens within the boundary layer where the high velocity gradients exist, it is natural to think that the wake and its entropy generation is a consequence of the moving wing disturbing the flow. It is also natural to think that wings with different lift distributions produce wakes with different levels of entropy generation and there may be a connection between entropy generation rates over the wing surface and in the wake. Therefore, to account for both cause and effect, volume integrals of the total entropy generation rates were computed during post-processing:

$$(\dot{S}_{gen})_{total} = \iiint_V \dot{S}_{gen} dv \quad (6.4)$$

It is interesting to note that for steady motion the theoretical value of this quantity should be related to the power consumed by the moving wing and the reference temperature by the following simple expression:

$$\left(\dot{S}_{gen}\right)_{total} = \frac{DU_{\infty}}{T_0} \quad (6.5)$$

This equation simply says that the power consumed by the horizontally moving, unaccelerated wing,  $DU_{\infty}$  should equal to the exergy destruction,  $T_0 \left(\dot{S}_{gen}\right)_{total}$ . Total drag,  $D$ , was approximated from the total drag coefficient directly from AVUS. Therefore equation 6.5 only provides an approximate value to which the results can be compared. Table 6.4 tabulates both the reference values and the CFD result.

Notice the significant differences between the expected values and the results from CFD. This could be due to several reasons: First of all, according to the flat plate boundary layer theory, this problem should contain laminar region up to roughly 11% of the chord, and transition and turbulent region elsewhere. Solving such flow with laminar Navier-Stokes equations assumes laminar flow everywhere in the computational domain and therefore loses the effect of turbulence. Secondly, the equation for total entropy generation rate (Eq.6.2) only accounts for the molecular viscosity. In CFD, Reynolds Averaging Navier-Stokes (RANS) types of equations tend to dissipate a lot of small scale structures in the flow. This leads to simplified flow field and gradients, and apparently inaccurate entropy generation predictions. There exists a concept of effective viscosity in turbulence models for RANS solvers. Its purpose is to recover the lost effect of those small-scale structures. The effective viscosity is known to be up to two orders of magnitude greater than the absolute viscosity. Since the effective viscosity value was not implemented in these entropy computations (equation 6.2), this important concept will be investigated in the future work.

## DISCUSSION

---

As noted earlier, computational and time constraints limited our study significantly. This led to under-refined areas within the grid and undesirable growth rates in the outer region as well as very large cells near the leading edge of the wing. These factors should be kept in mind when examining the results of this study.

As mentioned in the results section, the lift values from the CFD simulations compared favorably with the theoretical values from the lifting line theory. The induced drag values were calculated to be lower in both cases as compared to the theoretical values. The parabolic case resulted in the lower induced drag than the elliptic case, which disagrees with the classical lifting line theory.

Induced drag is not very easily extracted from a CFD simulation. Surface integration only yields the total drag from the pressure and the skin friction. Thus it is not possible to extract only the induced drag contribution from the surface integration. Trefftz plane method, on the other hand, attempts to calculate the induced drag from the lateral velocity perturbations caused only by the source of induced drag. The difficulties, however, of applying this method to a viscous CFD results were demonstrated in this project. As expected, the calculated induced drag was smaller than the theoretical values, possibly due to dissipated lateral velocity perturbations. We expected that the induced drag will further decrease with the distance from the wing. This is indeed the case as seen in Figure 7.1, which shows how the induced drag coefficient decreases as the Trefftz plane is moved further downstream. Figure 7.1 also shows the effect that the area of the Trefftz plane has on the induced drag calculations. All Trefftz planes extended six meters in the spanwise direction but were varied in the vertical direction. This was done to see the effect the area of the Trefftz plane has on the calculations. The Trefftz plane should not extend to the very course outer regions to avoid the contamination from the large cells and the boundary condition. Therefore an appropriate sized Trefftz plane needs to be found. It is apparent from the results shown in Figure 7.1 that a future study needs to investigate this further to find a good balance in the Trefftz plane area.

The steep drop in the induced drag coefficients at small streamwise distances in Figure 7.1 can be attributed to the fact that the streamwise velocity perturbation is not relatively small close to the wing. This negates the use of the integral of the lateral velocity perturbations, which assumes the negligible streamwise velocity perturbation. A modified Trefftz plane approach should be used in these regions in which the streamwise velocity perturbation is subtracted from the lateral velocity perturbations. After about five meters the slope of the curves becomes essentially constant. This constant decrease in this region can be attributed to the viscous effect.

Calculated entropy production rates deviated significantly from the expected values. As mentioned in the results, the viscosity value used in equation 6.2 may not be accurate. Further investigation using the effective viscosity in the turbulence cases will be performed. At present AVUS does not have capability for this calculation. However from other studies concerning 2D airfoils it has been seen that the effective viscosity can be as much as 100 to 400 times higher than the natural viscosity in some cells. This would place our entropy predictions close to similar order of magnitude as the expected values.

A computational domain in any CFD simulation cannot be infinite. When modeling airfoils and finite wings it is desirable to have the top, bottom, front, and side faces in the freestream region. Having the back face in the freestream region may require too many grid points. Therefore it may be possible that the wake and trailing vortex sheet may extend beyond the back face. Thus the volume integration may not capture all of the entropy production caused by the wing. Depending on how much entropy is being produced in the wake, this could cause the entropy production values calculated from the CFD simulations to deviate significantly from the expected values. When comparing two wings, however, this should not matter as long as the domains are of equal shape and volume.



## CONCLUSION

---

We conducted this study over the summer of 2004. A technique to create twisted wing geometries to give a desired lift distribution was demonstrated. A grid to capture the important flow physics was generated on the twisted wings. With this gridding methodology we obtained the accurate lift values, but the drag predictions were shown to be only reasonable. We have also demonstrated the method of Trefftz plane to calculate the induced drag. This method resulted in fairly accurate results for induced drag.

Some interesting results were obtained from the CFD simulations. One of them is that the parabolic case gave less induced drag than the elliptic case. This goes against the classical lifting line theory which says the elliptic lift distribution yields the minimum induced drag. Also the parabolic case gave a lower entropy production than the elliptic case. This agrees with Greene's [9] hypothesis that says that parabolic lift distribution will yield minimum entropy generation. However, it is important to note that the solutions are neither fully converged nor grid independent. The actual lift distributions were not verified and will be a focus of future work. At best, we have developed the necessary methodology to proceed into the work to follow.

## FUTURE WORK

---

Since computational restraints hindered grid quality and cell count, grid independence studies were not possible. This will be the focus of future work. We will conduct further CFD simulations using Fluent which allows for solution-adaptive grid refinement by adding cells in the area of interest.

Fluent also has the ability to allow the user to add cells anywhere in the domain. This feature should help improve grid quality in areas that have large jumps in cell size. Performing this task in Fluent allows the user to add grid points in a specified region and not affect any other region within the domain. This allows for efficient grid refinement and should help with solution convergence which was not achieved during the summer of 2004.

We will also attempt to evaluate the actual lift distribution that the wings are producing to see the validity of the lifting-line theory and our model generation technique.

To give more than two data points linking drag with exergy destruction, a wing with an arbitrary lift distribution will be modeled. This wing will be constructed to give the same total lift and will be composed of the same airfoil sections used in this study. Doing this will provide more insight into the connection between drag and exergy destruction.

We expect that the future work will yield grid independent, converged solutions of the cases performed thus far. From this, the drag, entropy production and exergy destruction rates will be related in terms of thermodynamic quantity. Using these results, we can then proceed to validate the classical lifting-line theory.

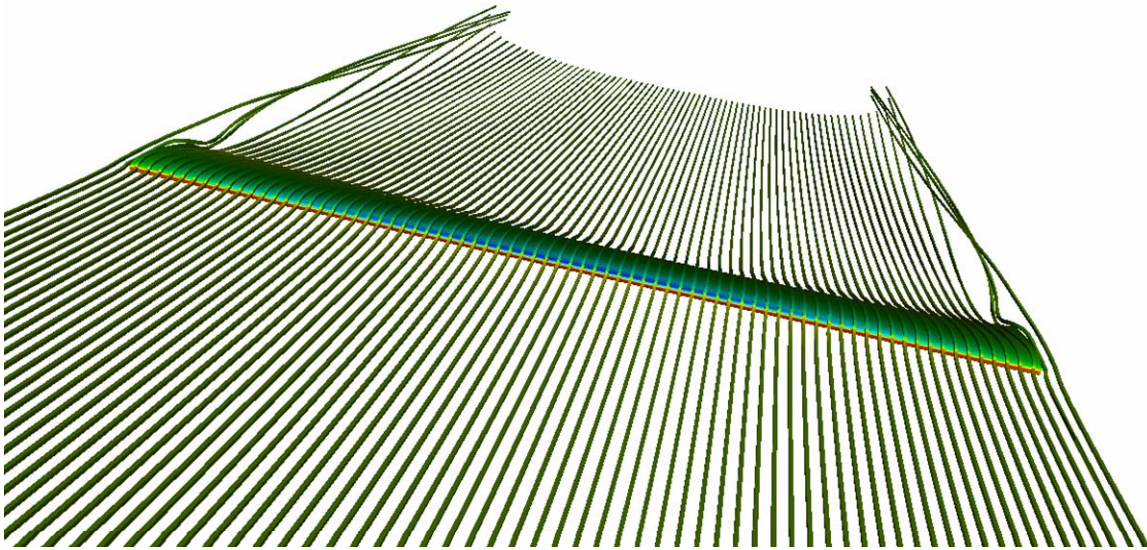


**Figure 6.4(a):** Rolled up streamlines for elliptic case

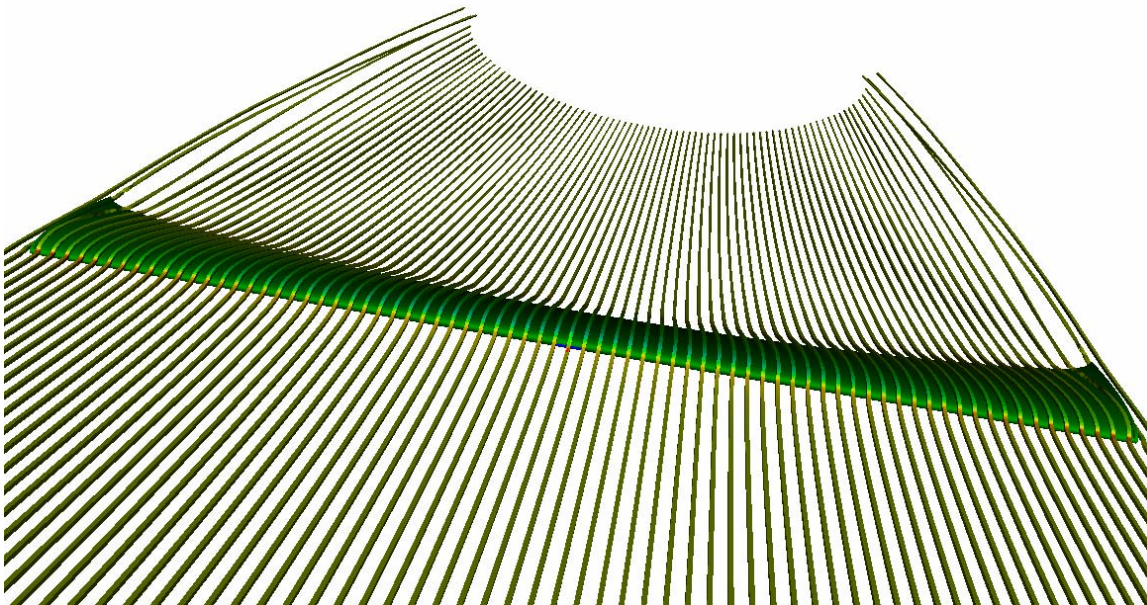


**Figure 6.4(b):** Rolled up streamlines for parabolic case

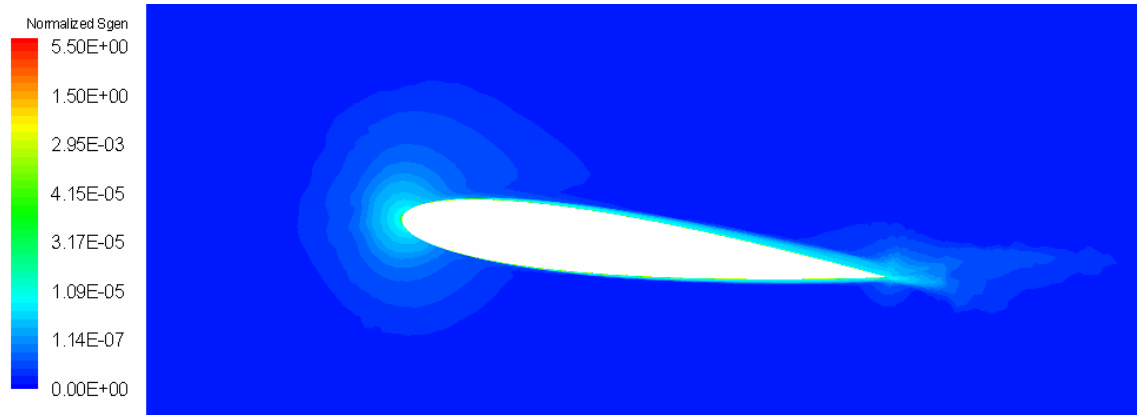


**Figure 6.5:** Total entropy generation rate for elliptic turbulent case at  $z = 0.5\text{m}$

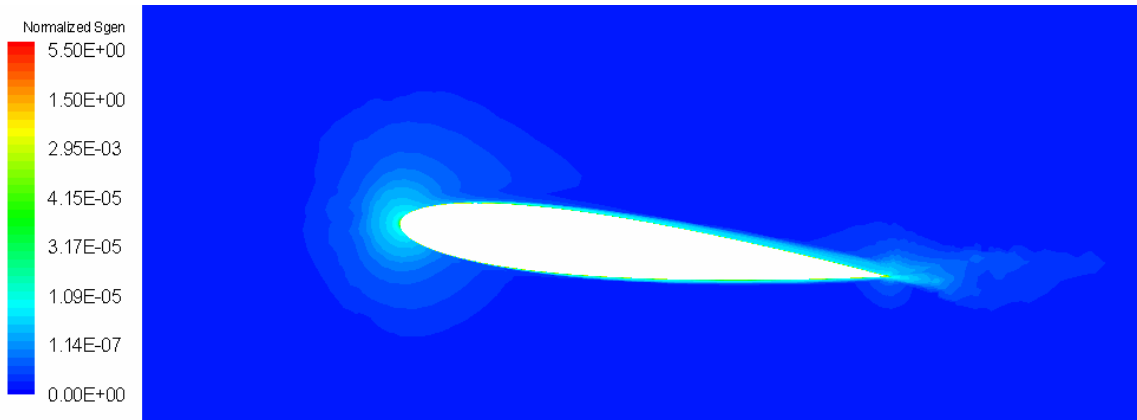


**Figure 6.6:** Total entropy generation rate for elliptic turbulent case at  $z = 1.5\text{m}$

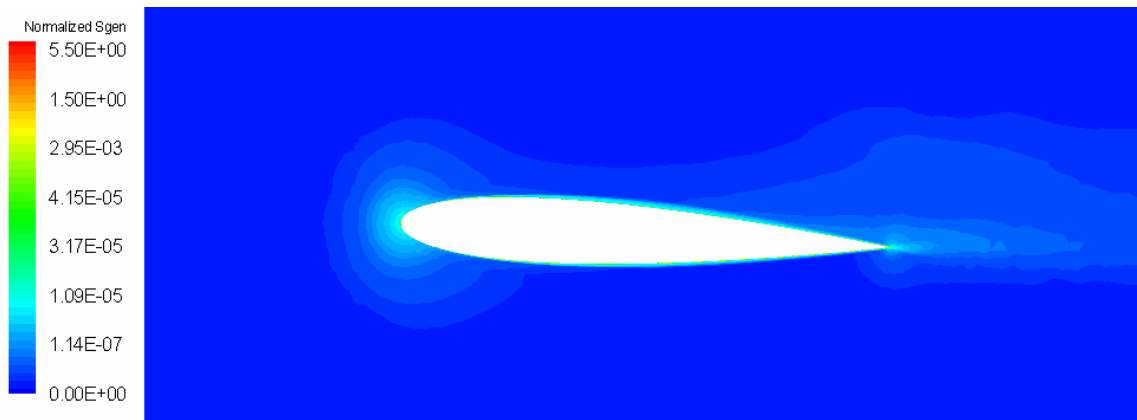


**Figure 6.7:** Total entropy generation rate for elliptic turbulent case at  $z = 2.9\text{ m}$

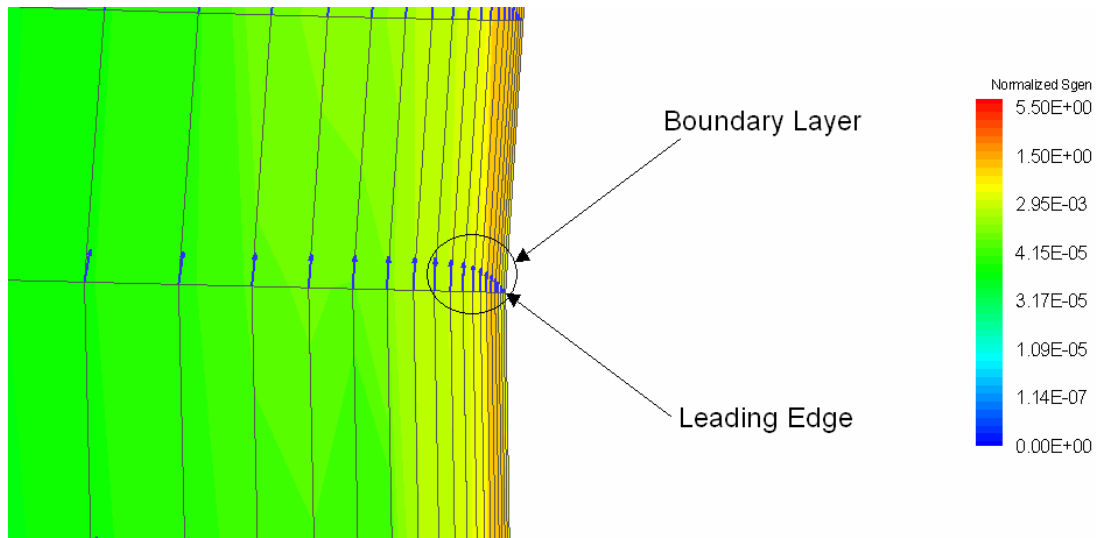


**Figure 6.8:** Total entropy generation rate at leading edge for elliptic turbulent case at  $z = 2.9$  m

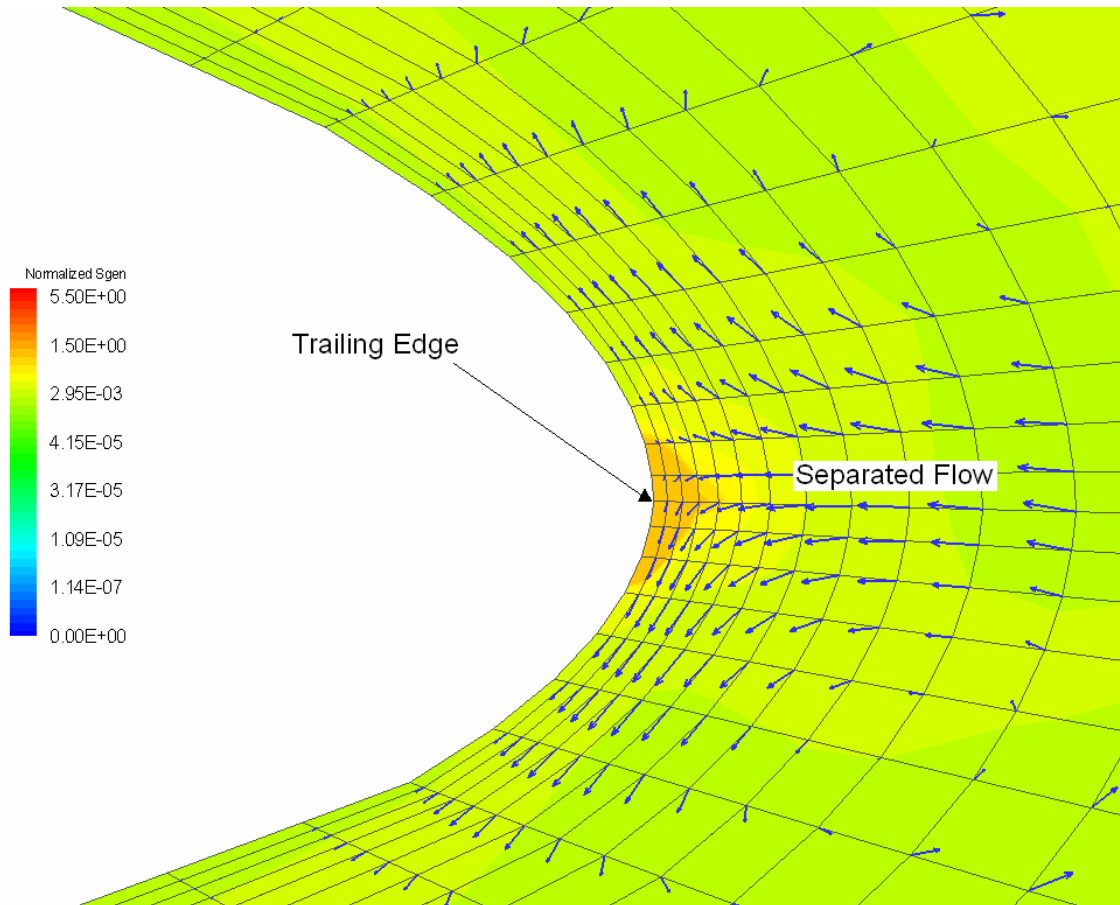


**Figure 6.9:** Total entropy generation rate at trailing edge for elliptic turbulent case at  $z = 2.9$  m

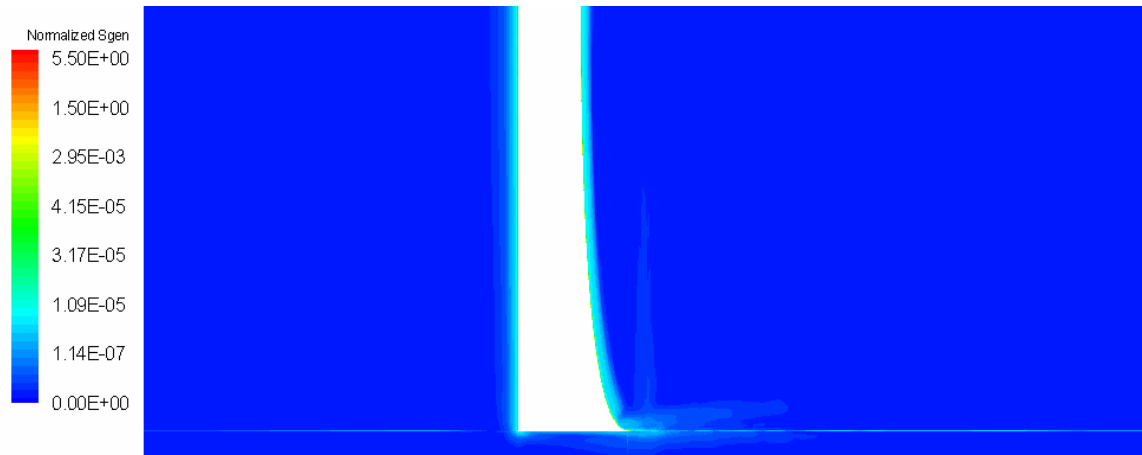


**Figure 6.10:** Total entropy generation rate for elliptic case at  $y = 0\text{m}$  (top view).

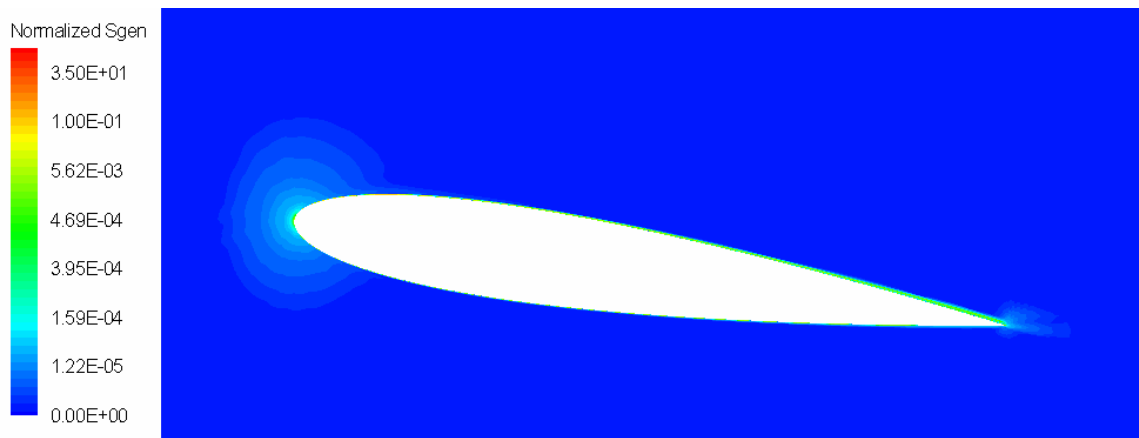


**Figure 6.11:** Total entropy generation rate for parabolic case at  $z = 0.5\text{m}$

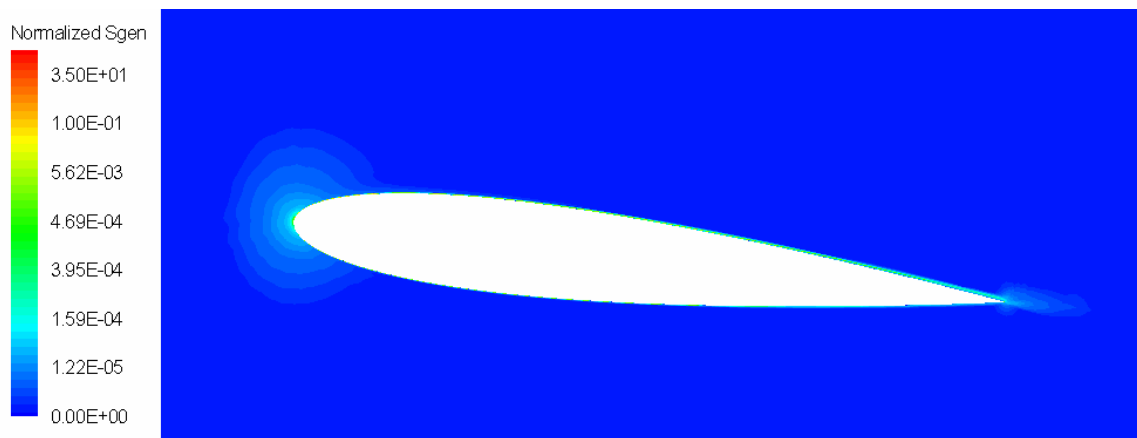


**Figure 6.12:** Total entropy generation rate for parabolic case at  $z = 1.5\text{m}$

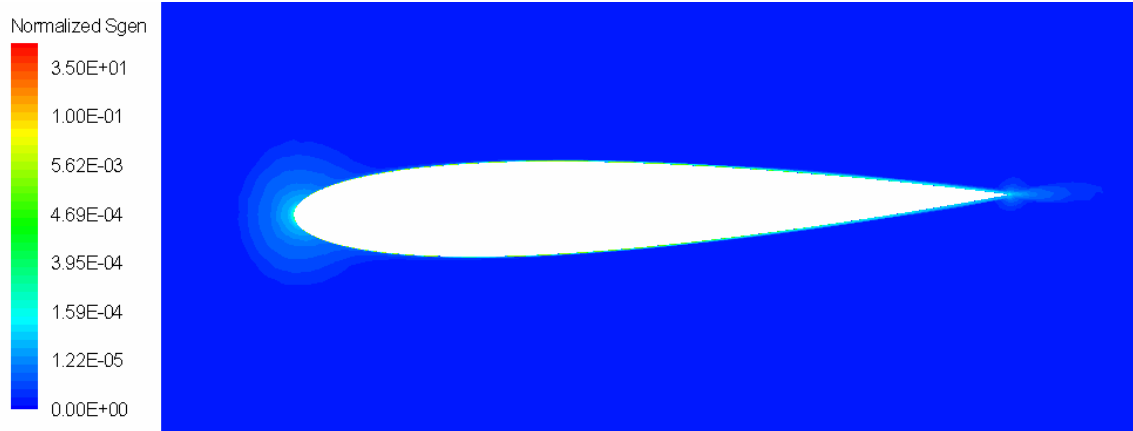


**Figure 6.13:** Total entropy generation rate for parabolic case at  $z = 2.9\text{m}$

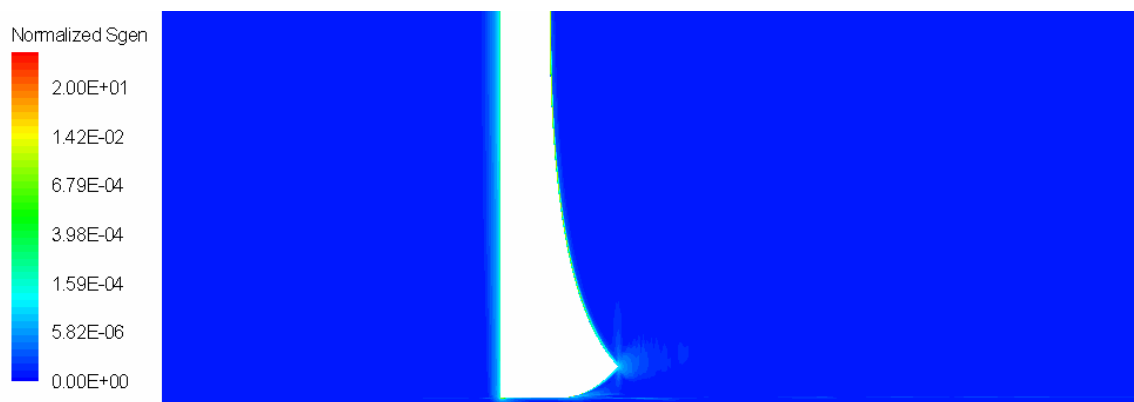


**Figure 6.14:** Total entropy generation rate for elliptic case at  $y = 0\text{m}$

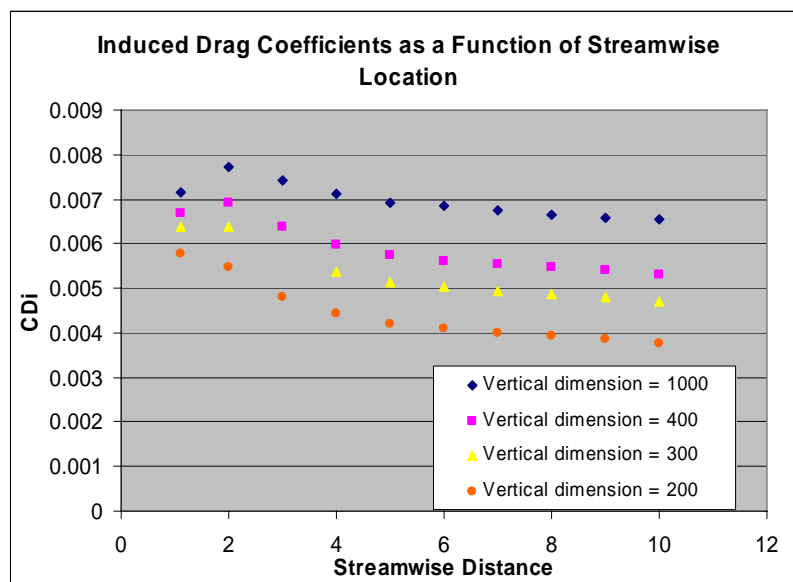


**Figure 7.1:** Induced drag coefficients at varying streamwise locations with varying Trefftz plane area (Elliptic Turbulent Case)

	$C_{Di}$		$C_D$ (Surface Integration)
	Lifting-Line	Trefftz Plane	
Elliptic Laminar NS	0.009839	0.007909	0.027967
Elliptic $k\omega$		0.008127	0.015342
Parabolic Laminar NS	0.010956	0.006933	0.016550
Parabolic $k\omega$		0.007754	0.017092

**Table 6.1:** Induced and total drag coefficients

	$C_L$	
	Lifting-Line Theory	Surface Integration
Elliptic Laminar NS	0.43064	0.42644
Elliptic $k\omega$		0.40499
Parabolic Laminar NS	0.43064	0.44475
Parabolic $k\omega$		0.43673

**Table 6.2:** Induced and total drag coefficients

	Elliptic		Parabolic	
	Laminar	Turbulent	Laminar	Turbulent
$C_{D,press}$	$2.7413 \times 10^{-2}$	$1.1152 \times 10^{-2}$	$1.2602 \times 10^{-2}$	$1.2621 \times 10^{-2}$
$C_{D,friction}$	$5.5440 \times 10^{-4}$	$4.1898 \times 10^{-3}$	$3.9471 \times 10^{-3}$	$4.4766 \times 10^{-3}$
$C_{D,total}$	$2.7967 \times 10^{-2}$	$1.5342 \times 10^{-2}$	$1.6550 \times 10^{-2}$	$1.7092 \times 10^{-2}$
$C_{L,press}$	$4.2627 \times 10^{-1}$	$4.0516 \times 10^{-1}$	$4.4489 \times 10^{-1}$	$4.3689 \times 10^{-1}$
$C_{L,friction}$	$1.7429 \times 10^{-4}$	$-1.7116 \times 10^{-4}$	$-1.3489 \times 10^{-4}$	$-1.6052 \times 10^{-4}$
$C_{L,total}$	$4.2644 \times 10^{-1}$	$4.0499 \times 10^{-1}$	$4.4475 \times 10^{-1}$	$4.3673 \times 10^{-1}$

**Table 6.3:** Drag and lift coefficients calculated with surface integration over the wing surface



	<b>Parabolic</b>		<b>Elliptic</b>	
<b>Total Sgen Rate</b>	Laminar	Turbulent	Laminar	Turbulent
Expected Values (W/K)	66.4	68.6	112.2	61.56
CFD Results (W/K)	0.63758	0.42924	1.23474	0.46412

**Table 6.4:** Expected total entropy generation rate and the results from the CFD simulations

## REFERENCES

---

- [1] Moorhouse, D., “Proposed System-Level Multidisciplinary Analysis Technique Based on Exergy Methods”, *Journal of Aircraft* Vol.40, No.1, January-February 2003.
- [2] Bejan, A., “Constructal Theory: Tree-Shaped Flows and Energy Systems for Aircraft”, *Journal of Aircraft* Vol. 40, No. 1, January-February 2003.
- [3] Paulus, D., and Gaggioli, R., “Rational Objective Function for Vehicles”, *Journal of Aircraft* Vol.40, No. 1 January-February 2003.
- [4] Roth, B., and Mavris, D., “Generalized Model for Vehicle Thermodynamic Loss Management”, *Journal of Aircraft* Vol.40, No. 1 January-February 2003.
- [5] Roth, B., and Mavris, D., “Method for Propulsion Technology Impact Evaluation via Thermodynamic Work Potential”, *Journal of Aircraft* Vol.40, No. 1 January-February 2003.
- [6] Danner, T., and Mavris, D., “Foundational Concepts for a Work Potential-Based Design Methodology”, AIAA Technical Paper No. 2003-6707.
- [7] Danner, T., Marvis, D., “Foundational Concepts for a Work Potential-Based Design Methodology”, AIAA Technical Paper No. 2003-6707.
- [8] Simpson, M., and Kay, J., *Availability, Exergy, the Second Law and all that....* 1989  
<<http://www.fes.uwaterloo.ca/u/jjkay/pubs/exergy/index.html>>
- [9] Greene, G., “An Entropy Method For Induced Drag Minimization”, Technical Paper Series No. 89-2344.
- [10] Mavriplis, D., *Aerodynamic Drag Prediction using Unstructured Mesh Solvers*. National Institute of Aerospace.
- [11] Strang, W. Z., *Cobalt<sub>60</sub>: User’s Manual*. Air Force Research Laboratory, CFD Research Branch, Wright-Patterson Air Force Base, Sept. 2000.
- [12] Bourdin, P., “Planform Effects On Lift-Induced Drag”, AIAA Technical Paper No. 2002-3151.
- [13] White, F., *Viscous Fluid Flow*. McGraw-Hill Inc., New York, 1994, pp. 471-479.
- [14] Hunt, D., Cummings, R., and Giles, M., “Wake Integration for Three-Dimensional Flowfield Computations: Applications”, *Journal of Aircraft* Vol. 36, No. 2, March-April 1999.
- [15] Bourdin, P., *Numerical Prediction of Wing-Tip Effects On Lift-Induced Drag*. International Council of the Aeronautical Sciences, 2002.